Journal of Sound and Vibration 619 (2025) 119374

Contents lists available at ScienceDirect

Journal of Sound and Vibration

journal homepage: www.elsevier.com/locate/jsvi

Dynamic modeling and analysis for the identification of gear localized faults in planetary gearboxes under eccentricity effects

Jiawei Fan [a,b], Yu Guo [a,*], Enrico Zio [b,c], Hugo Andre [d], Jing Na [a], Xingchao Yin [a]

[a] *Faculty of Mechanical and Electrical Engineering, Kunming University of Science and Technology, Kunming 650500, China*
[b] *Department of Energy, Politecnico di Milano, Milan 20156, Italy*
[c] *Centre de Recherche sur les Risques et les Crises (CRC), MINES Paris-PSL, Sophia Antipolis 06560, France*
[d] *Laboratoire d'Analyse des Signaux et des Processus Industriels, EA3059, Universite Jean Monnet de Saint-Etienne, Universite de Lyon, Roanne 42334, France*

ARTICLE INFO

Keywords:
Planetary gearboxes
Gear localized fault
Dynamic model
Instantaneous angular speed
Time-varying mesh stiffness
Gear eccentricity

ABSTRACT

Planetary gearboxes are widely used in heavy industries such as wind power, transportation, and manufacturing, and their reliability is critical for ensuring the stable operation of mechanical systems. Fault detection and diagnosis in planetary gearboxes are important for ensuring system safety. In gear transmission systems, the features of localized faults typically manifest as sidebands around the meshing frequency in the spectrum or as gear rotation frequency in the envelope spectrum. However, factors such as gear eccentricity and shaft runout can also produce localized gear fault-like spectral features. This makes it difficult to detect localized faults based on characteristic spectral line analysis and sideband energy ratio, especially in complex systems like planetary gearboxes. Recently, the instantaneous angular speed (IAS) signal has emerged as a promising alternative, offering advantages such as eliminating the need for order tracking and being unaffected by time-varying signal transmission paths in planetary gear sets. In this work, we develop a modified planetary gearbox dynamic model and investigate the effects of gear fault and eccentricity on mesh stiffness. Utilizing the developed model, IAS signals are generated, and their waveforms and order spectra analyzed. Additionally, we propose an abnormal-preserving spectral component reconstruction method to extract and enhance abnormal components within the signal. The results indicate that localized gear fault and eccentricity exhibit the same periodicity, both generating fault-related sidebands around meshing orders in the order spectrum, and fault characteristic components in the envelope spectrum. However, after abnormal component reconstruction, gear faults exhibit distinct periodic jitters, accompanied by a significant increase in kurtosis. In contrast, the kurtosis of the reconstructed signal in the case of gear eccentricity does not show a noticeable increase. This distinction allows the accurate identification of gear localized fault in gear systems. The findings are validated experimentally on a planetary gearbox test rig.

1. Introduction

The planetary gearbox has numerous advantages, such as a large load capacity, high transmission ratio, and smooth operation, which makes it widely used, e.g., in wind power [1,2], and transportation [3–5] applications. However, due to the complexity and severity of the working conditions, gear faults, such as pitting, wear and cracks, may occur [6]. If the fault is severe, it may lead

* Corresponding author.
E-mail address: guoyu@kust.edu.cn (Y. Guo).

https://doi.org/10.1016/j.jsv.2025.119374
Received 14 April 2025; Received in revised form 23 June 2025; Accepted 4 August 2025
Available online 14 August 2025

to production interruptions and even accidentally casualties. Therefore, condition monitoring, and fault detection and diagnosis of planetary gearboxes are extremely important for the reliability and safety of the power transmission system.

Most of the signal processing methods for fault diagnosis of planetary gearboxes are based on vibration signal [7–11], acoustic emission (AE) [12,13] and current [14] signals. However, these methods often face the disadvantages of serious signal modulation and acquire complex signal processing [15,16]. Recently, instantaneous angular speed (IAS) signals provide rich fault information in rotating machinery because of the close correlation with torsional dynamics, it has been adopted for fault detection in gear-containing systems. The torque is transmitted through gear meshing and directly reflected in the IAS, which are acquired using rotary encoders with equal-angle sampling, eliminating the need for order tracking [17]. These advantageous characteristics have made IAS-based signal processing an effective way for fault detection in rotating machinery, including bearings [18–20], gears [17,21] and spindles [22]. Zhao et al. [23] proposed a kurtosis-guided local polynomial differentiator (KLPD) to estimate the IAS based on the encoder signal and, then, identify gear faults through the waveform of IAS. Zeng et al. [24] developed a dual detector self-denoising method to suppress the false IAS caused by encoder errors, enabling fault diagnosis of planetary gearboxes from the IAS order spectra. Feng et al. [25] demonstrated that rotary encoder signals are free from additional amplitude modulation caused by vibration signal time-varying transmission paths, making IAS more suitable for fault detection in planetary gearboxes. For both vibration, AE and IAS signals, localized gear faults typically manifest as sidebands around the meshing frequency in the spectrum or as the gear rotation frequency in the envelope spectrum within gear transmission systems. However, factors such as shaft runout and gear eccentricity can also produce spectral features similar to those of gear faults [26]. This complicates the detection of localized gear faults based solely on spectral analysis and sideband energy ratio related with fault characteristic frequencies, especially in complex systems like planetary gearboxes. Therefore, it is not sufficient to assume that the mere presence of these frequency components in the order spectrum indicates a localized gear fault. Therefore, it is important to investigate the distinctive characteristics of IAS signals corresponding to localized gear faults and gear eccentricity. This will help guide the development of more targeted fault feature extraction methods and algorithms for planetary gearboxes.

It is well known that establishing a mechanical system dynamics model with fault parts and conducting dynamic characteristic analysis is one of the effective and crucial approaches to assist in developing and validating fault diagnosis methods [27–29]. However, current research related to the dynamic characteristics of planetary gearboxes is mainly associated with vibration signals under normal and gear fault condition. For example, Liang et al. [30] developed a dynamic model incorporating the effect of multiple vibration sources and the effect of the transmission path, to model the vibration signals of a planetary gearbox and investigate the vibration properties in the healthy condition and in the cracked tooth condition. Han et al. [31] established an improved lumped parameter dynamic model and observed the amplitude modulation phenomenon and the frequency modulation phenomenon in the simulated results. Jiang et al. [32] proposed a dynamic model of a planetary gearbox with localized gear faults using time-varying mesh stiffness [33,34] as the main excitation source, and analyzed the spectral characteristics of vibration signals under fault conditions. Hu et al. [35] added the bearing stiffness formula into the gear system model and proposed a translational-torsional model for the planetary gear set, and eventually analyzed the time-domain and frequency-domain symptoms of vibration to improve the recognition of the fault mechanism. Qin et al. [36] used a time-varying mesh stiffness model incorporating time-varying friction to study the effects of varying degrees of pitting at different locations, illustrating the roles of both mesh stiffness and friction excitation in the dynamic responses of planetary gearboxes. Although some of these works on the dynamic modeling of planetary gearboxes include torsional dynamics, they do not analyze torsional direction signals and lack a detailed force analysis of the planet gears. For instance, they directly adopt a force analysis method that examines the forces on the planet gears as the moment of inertia of the planet gears and two meshing forces (external meshing between the sun gear and the planet gear, and internal meshing between the ring and planet gear). Although such equilibrium differential equations of a mechanical system may have a solution, the resulting calculations are likely to be inaccurate. This is because, unlike the sun gear, which transmits torque to the planet gear via gear meshing, the planet gears transmit torque to the carrier through the planet shafts, driving the carrier to rotate around its center. This requires a tangential force centered at the carrier's center, with the radius being the distance from the planet gear's center to the carrier's center, and the direction tangential to the carrier's rotation. Moreover, these models do not consider the effect of gear eccentricity on the signal. They also lack a comparative analysis of the dynamic behaviors and signal characteristics associated with localized gear fault and eccentricity.

To address these issues, we establish a modified lumped-parameter model of the planetary gear sets that simulates IAS signals of each rotating part, including the sun, the planets, the ring and the carrier. The effect of localized gear fault and gear eccentricity on the time-varying mesh stiffness of gears is analyzed. Then, IAS signals of the planetary gear sets are simulated using time-varying mesh stiffness as the excitation, and the obtained simulated signals are analyzed in both the waveform and order domains to investigate the effect of gear fault and shaft eccentricity on IAS dynamic behavior. In addition, to extract and enhance abnormal components in the signal for improved identification of gear fault and eccentricity, we propose an abnormal-preserving spectral component reconstruction method. Analysis of simulated IAS signals under different conditions reveals that localized gear fault and eccentricity share the same periodicity in the IAS waveform, and both generate fault-related sidebands around meshing orders in the order spectrum and fault characteristic components in the envelope spectrum. After abnormal component reconstruction, gear faults appear as obvious periodic jitters with a higher kurtosis value.

The main innovations and contributions of this paper are as follows:

- The effect of gear eccentricity on the time-varying mesh stiffness is analyzed, the pure torsional lumped-parameter dynamic model of the planetary gearbox is improved, and IAS dynamic behavior under gear fault and eccentricity conditions is investigated.

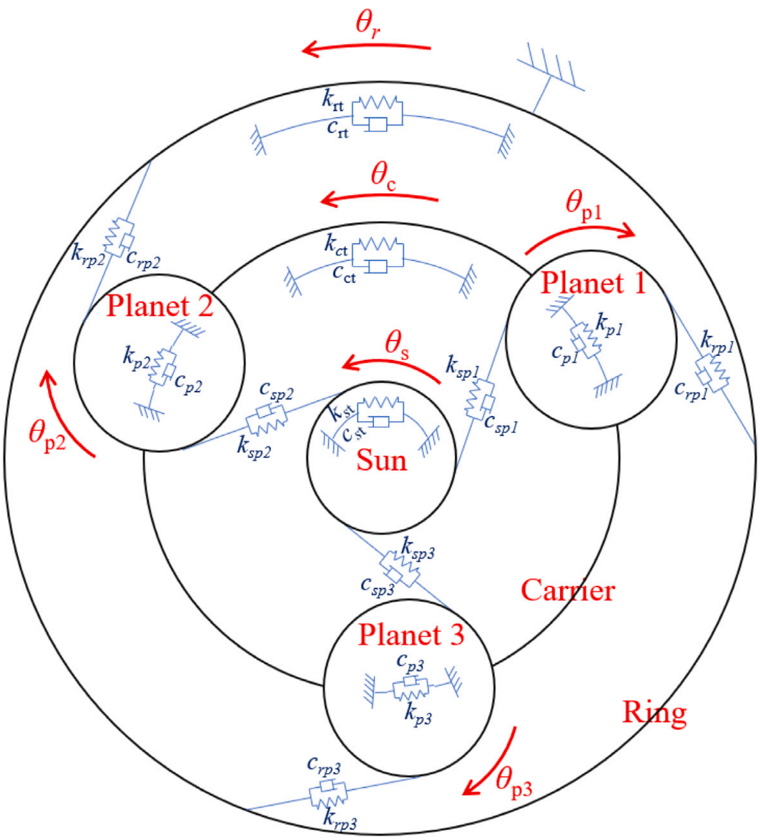

Fig. 1. Lumped-parameter-model of the planetary gear sets.

- An abnormal-preserving spectral component reconstruction method is proposed to effectively distinguish identical order/frequency components generated by different excitations, such as localized gear faults and gear eccentricity.

The remaining sections of this paper are organized as follows. Section 2 presents a modified lumped-parameter pure torsional dynamic model of a planetary gear set. Section 3 analyzes the effect of gear fault and gear eccentricity on time-varying mesh stiffness. Section 4 utilizes the time-varying mesh stiffness under different conditions as the excitation for the modified dynamic model to generate IAS simulation signals, followed by an analysis of IAS dynamic behavior under various conditions. Section 5 introduces the abnormal-preserving spectral component reconstruction method and applies it to process the simulated IAS signals. Section 6 provides experimental validation. Finally, Section 7 summarizes the conclusions.

2. Modified lumped-parameter model for planetary gear set

The IAS signal of a planetary gearbox is closely related to the torque transmitted by its rotating components. In a planetary gearbox, the torques acting on each component differ and interact with one another. Therefore, it is necessary to analyze the torque distribution across the different components of the planetary gear sets. By examining the relationship between torque and IAS, the dynamic behavior and characteristics of the IAS signals can be studied.

2.1. IAS dynamics analysis of planetary gear set

To focus on the IAS components corresponding to each rotating part in planetary gear sets during the gear meshing process and to reasonably simplify the dynamic model, the following assumptions are made: (1) the modeling only considers rotational degrees of freedom, where the sun, the planet, the ring gear and the carrier are treated as rigid bodies. The weight of the shafts and the box are evenly distributed to the sun gear, the planet gears, the ring gear and the carrier, respectively; (2) the parts are modeled as circular mass blocks with a diameter equal to the diameter of the base circle; (3) the interaction between gear meshes is modeled using spring force that acts along the line of action. The simplified model does not take into account the subordinate interference factors such as backlash, meshing friction, transmission errors, manufacturing and assembly errors; (4) The damping used in the dynamic model is represented by the damping coefficient, and this type of damping is viscous damping.

A modified lumped-parameter model is established for a 2K-H planetary gear set as depicted in Fig. 1. The model consists of one sun gear s, one ring r, one carrier c and three equally-spaced planets p_i, (i = 1, 2, 3). In the established lumped-parameter model, the torque is introduced through the sun gear shaft and transmitted through the carrier to the output shaft. In this model, the ring gear is fixed in place on the gearbox, whereas the other components rotate around their respective centers. The parameters θ_s, θ_c, and θ_r represent the angular displacements of the sun gear, ring and carrier around the center of the planetary gear sets. The symbol θ_{pi} (i = 1, 2, 3) indicates the rotation angular displacement of the ith planet around its center. The parameters k_{spi} and c_{spi} denote the mesh stiffness and meshing damping of the meshing point of the sun gear and the ith planet, respectively. Similarly, k_{rpi} and c_{rpi} stand for the mesh stiffness and meshing damping of the meshing point of the ring and the ith planet, respectively. The symbols k_{jt} and c_{jt} (where j = s, r, c) denote the torsional stiffness and torsional damping of the sun gear, ring and carrier, respectively; k_{pi} and c_{pi} represent the bending stiffness and damping of the planet shaft, respectively. The mechanical analysis is conducted on each component in the model and presented below.

The rotation of the sun gear is driven by the torque provided by the motor connected to the sun gear shaft, and this torque is transmitted by meshing with three planets simultaneously. As a result, the force acting on the sun gear is balanced by the input torque, three meshing forces from the three meshing points between the sun gear and planets, the inertia moment of the sun gear, and the equivalent torsional stress of the sun gear shaft. The dynamic equation governing the IAS of the sun gear can be expressed as

$$(J_s/r_s)\ddot{\theta}_s + \sum_{n=1}^{3} c_{spi}(\dot{\theta}_s r_s+\dot{\theta}_{pi} r_p) + \sum_{n=1}^{3} k_{spi}(\theta_s r_s+\theta_{pi} r_p) + (c_{st}/r_s)\dot{\theta}_s + (k_{st}/r_s)\theta_s = T_{in}/r_s \tag{1}$$

where J_s denotes inertia of the sun gear, r_s and r_p represent the base circle radius of the sun gear and planets, and T_{in} denotes the torque input from the sun gear shaft.

A planetary gear set typically consists of multiple planets. Each planet is subject to two meshing forces: one at the sun gear-planet gear meshing point, which drives the planet to rotate around its own center, and the other at the ring-planet gear meshing point, which drives the planet to rotate around the center of the planetary gear set. The combined force of the two meshing forces causes the planet shaft to push the carrier to rotate, which is overlooked in the existing works on the pure torsional dynamic model of the planetary gear set. After reanalyzing the torque balance, each planet is subject to two meshing force and the tangential pressure forces from the carrier, balanced by the inertia moment of the rotation of the planet. Thus, the IAS dynamic equation of planets can be expressed as

$$\begin{aligned}&(J_p/r_p)\ddot{\theta}_{pi} + c_{spi}(\dot{\theta}_{pi} r_p + \dot{\theta}_s r_s) + k_{spi}(\theta_{pi} r_p + \theta_s r_s)\\ &+ c_{rpi}(\dot{\theta}_{pi} r_p - \dot{\theta}_r r_r) + k_{rpi}(\theta_{pi} r_p - \theta_r r_r) + (c_{pi} r_c)\dot{\theta}_c + (k_{pi} r_c)\theta_c = 0\end{aligned} \tag{2}$$

where J_p denotes the inertia of the planet, and r_r represents the base circle radius of the ring.

Although the ring is fixed to the gearbox, it is subjected to meshing forces at the ring-planet gear meshing points. To balance the meshing force, the ring gear generates a reaction force. This reaction force is balanced by the meshing forces from three ring-planet gear meshing points, the torsional stress of the ring, and the inertia moment during the torsional vibration of the ring. Hence, the IAS dynamic equation of the ring can be expressed by

$$(J_r/r_r)\ddot{\theta}_r + \sum_{n=1}^{3} c_{rpi}(\dot{\theta}_r r_r-\dot{\theta}_{pi} r_p) + \sum_{n=1}^{3} k_{rpi}(\theta_r r_r-\theta_{pi} r_p) + (c_{rt}/r_r)\dot{\theta}_r + (k_{rt}/r_r)\theta_r = 0 \tag{3}$$

For the carrier, its rotation is driven by the resultant force formed by the tangential forces of the three planet shafts. The balance of the carrier is achieved by the tangential resultant force of the three planet shafts, the torsional stress of the carrier shaft, the output torque and the inertia moment of the carrier itself. The tangential force of each planet shaft is the resultant force of the meshing force of two meshing points. Therefore, the IAS dynamic equation of the carrier can be expressed as

$$\begin{aligned}&(J_c/r_c)\ddot{\theta}_c + \sum_{n=1}^{3} c_{spi}(\dot{\theta}_s r_s+\dot{\theta}_{pi} r_b) + \sum_{n=1}^{3} k_{spi}(\theta_s r_s+\theta_{pi} r_b) + \sum_{n=1}^{3} c_{rpi}(\dot{\theta}_r r_r-\dot{\theta}_{pi} r_p)\\ &+ \sum_{n=1}^{3} k_{rpi}(\theta_r r_r-\theta_{pi} r_p) + (c_{ct}/r_c)\dot{\theta}_c + (k_{ct}/r_c)\theta_c = T_{out}/r_c\end{aligned} \tag{4}$$

where J_c denotes the inertia of the carrier, r_c represents the radius of the carrier and T_{out} denotes the torque output from the carrier shaft.

2.2. Parameters of the dynamic model

The structural parameters of the planetary gearbox can be obtained by consulting its drawings and manuals. The structural parameters of the planetary gear set used for simulation are listed in Table 1.

In addition to the fundamental structural parameters of the planetary gear set, it is crucial to take into account the equivalent torsional stiffness and damping of each component, along with the time-varying mesh stiffness and damping of each meshing pair. These parameters can be estimated using empirical formulas or mechanical methods.

According to the theoretical knowledge of elasticity, the equivalent torsional stiffness can be estimated in [37] by

$$k_t = \frac{GI_p}{l} = \frac{\pi G d^4}{32l} \tag{5}$$

Table 1
Structural parameters of the planetary gear set.

Parameters	Sun gear	Planets	Ring	Carrier
Teeth number	21	31	84	/
Module (mm)	1.5	1.5	1.5	/
Pressure angle (°)	20	20	20	/
Mass (kg)	2.12	0.32	0.58	4.79
Radius (mm)	15.75	23.25	63	39
Elastic modulus (MPa)	2.1×10^5			
Poisson's ratio	0.28			

where G denotes the shear modulus of the torsional material (GPa), d represents the diameter of the shaft and l is the length of the acting section (m). The equivalent torsional damping can be estimated as in [38] by

$$c_t = 2\xi_t\sqrt{k_t\frac{J_1J_2}{J_1+J_2}} \tag{6}$$

where ζ_t indicates the torsional damping ratio, k_t denotes the torsional stiffness, J_1 and J_2 are the inertia equivalent moments at both ends of a shaft. The time variation of meshing damping can be ignored [39], and the empirical formula of viscous damping of gear meshing can be estimated as in [40] by

$$c_m = 2\xi_m\sqrt{\bar{k}_m\frac{{r_1}^2J_1{r_2}^2J_2}{{r_1}^2J_1+{r_2}^2J_2}} \tag{7}$$

where ζ_m indicates the meshing damping ratio, k_m denotes the mesh stiffness, r_1 and r_2 are the base circle radii of the two meshing gears. J_1 and J_2 are the inertia moment of the two meshing gears.

The time-varying mesh stiffness plays an important role in the proposed dynamic model, which is discussed in the next section.

3. Time-varying mesh stiffness

3.1. Time varying mesh stiffness under gear healthy condition

The potential energy method assumes a gear tooth as a non-uniform cantilever beam and uses engineering beam theory to estimate the mesh stiffness. This method considers the total energy stored in a pair of teeth, including Hertzian contact energy, bending energy, shear energy and axial compressive energy, corresponding to Hertzian contact stiffness, bending stiffness, shear stiffness and axial compressive stiffness, respectively. For the gear, the analytical expressions of the Hertzian stiffness k_h, bending stiffness k_b, shear stiffness k_s and axial compressive stiffness k_a are derived in Ref. [33], which can be expressed by

$$k_h = \frac{\pi EL}{4(1-\upsilon^4)} \tag{8}$$

$$\frac{1}{k_\mathrm{b}} = \int_{-\alpha_1}^{\alpha_2}\left\{3\left[1+\cos\alpha_1\left(\left(\alpha_2-\alpha\right)\sin\alpha-\cos\alpha\right)\right]^2\cdot\left(\frac{\left(\alpha_2-\alpha\right)\cos\alpha}{\left[2EL\left(\sin\alpha+\left(\alpha_2-\alpha\right)\cos\alpha\right)^3\right]}\right)\right\}\mathrm{d}\alpha \tag{9}$$

$$\frac{1}{k_\mathrm{s}} = \int_{-\alpha_1}^{\alpha_2}\frac{1.2\,(1+\upsilon)\left(\alpha_2-\alpha\right)\cos\alpha\cos^2\alpha_1}{EL\left[\sin\alpha+\left(\alpha_2-\alpha\right)\cos\alpha\right]}\mathrm{d}\alpha \tag{10}$$

$$\frac{1}{k_a} = \int_{-\alpha_1}^{\alpha_2}\frac{\left(\alpha_2-\alpha\right)\cos\alpha\sin^2\alpha_1}{2EL\left[\sin\alpha+\left(\alpha_2-\alpha\right)\cos\alpha\right]^3}\mathrm{d}\alpha \tag{11}$$

where E and L represent Young's modulus and the tooth width, respectively, υ is the Poisson's ratio of the material, where α_1 is the angle between the acting force and tangent direction of the base circle, α_2 is the half tooth angle on the base circle of the external gear. The mesh stiffness of a single-tooth-pair can be determined using Eq. (12),

$$k_\mathrm{t} = \left(\frac{1}{k_\mathrm{h}}+\frac{1}{k_{\mathrm{b}_1}}+\frac{1}{k_{\mathrm{s}_1}}+\frac{1}{k_{\mathrm{a}_1}}+\frac{1}{k_{\mathrm{b}_2}}+\frac{1}{k_{\mathrm{s}_2}}+\frac{1}{k_{\mathrm{a}_2}}\right)^{-1} \tag{12}$$

where subscripts 1 and 2 relate to the driving gear and the driven gear, respectively. Considering the contact ratio of the spur gear is changed between one and two, the total time-varying mesh stiffness of the gear can be expressed by

$$k_\mathrm{t} = \sum_{i=1}^{2}\left(\frac{1}{k_{\mathrm{h},i}}+\frac{1}{k_{\mathrm{b}_1,i}}+\frac{1}{k_{\mathrm{s}_1,i}}+\frac{1}{k_{\mathrm{a}_1,i}}+\frac{1}{k_{\mathrm{b}_2,i}}+\frac{1}{k_{\mathrm{s}_2,i}}+\frac{1}{k_{\mathrm{a}_2,i}}\right)^{-1} \tag{13}$$

By substituting the parameters such as the number of gear teeth of each gear into Eq. (13), the time-varying mesh stiffness for one sun gear-planet gear meshing and one ring-planet gear meshing can be calculated. These results are shown in Figs. 2 and 3, respectively.

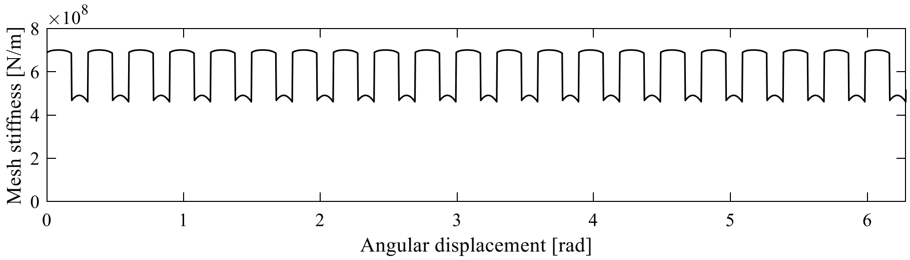

Fig. 2. Mesh stiffness of one sun gear-planet gear pair.

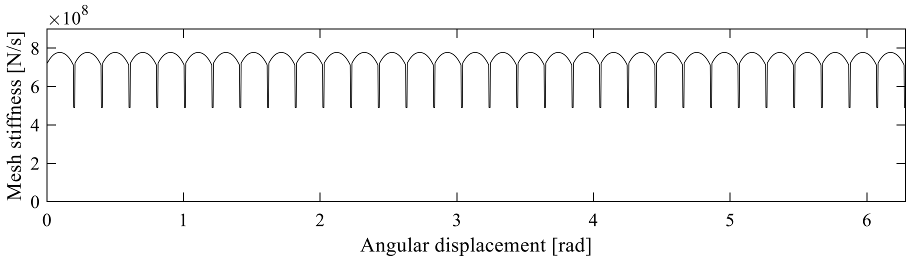

Fig. 3. Mesh stiffness of one planet gear-ring gear pair.

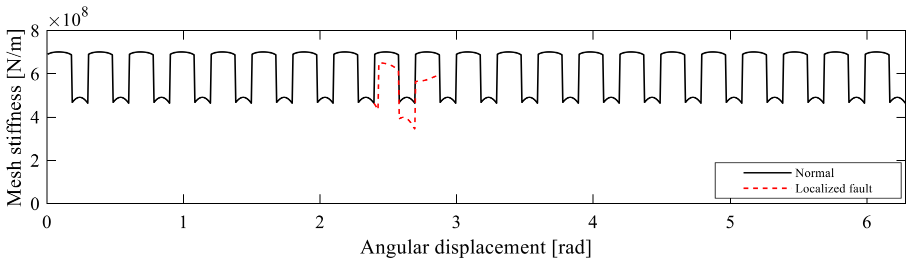

Fig. 4. Comparison of mesh stiffness under gear healthy condition and sun gear fault condition.

Because one sun gear meshes with three planet gears simultaneously, and there is phase difference among the three meshing points, the combined effect of the three meshing points ensures smoother meshing of the planetary gear train. The meshing points between the ring gear and the three planet gears achieve the same effect. The time-varying mesh stiffness of gears meshing is fitted using Fourier series, with the angle value serving as the variable. This fitted mesh stiffness is, then, used as the dynamic excitation for the dynamic model.

3.2. Time-varying mesh stiffness under sun gear localized fault condition

A localized gear fault refers to damage occurring on one tooth of the gear. When the faulty tooth engages in meshing, the gear's dynamic behavior exhibits abnormal variations. In contrast, during the meshing of the remaining healthy teeth, the gear maintains its steady-behavior under normal conditions. The localized fault such as tooth surface peeling is simulated by reducing the tooth thickness, which causes a decrease in the contact ratio when the faulted tooth engages in meshing, as well as a reduction in the length of the meshing line. Using the evaluation method of time-varying mesh stiffness in Eq. (13), the time-varying mesh stiffness of one sun-planet gear meshing pair under a sun gear tooth fault condition is obtained, as shown in Fig. 4. Compared to the healthy meshing condition, a sudden decrease of mesh stiffness can be observed at the position where the faulty tooth is involved in the meshing (see the red dashed line in Fig. 4).

3.3. Time-varying mesh stiffness under gear eccentricity condition

During the operation of a planetary gearbox, factors such as self-weight of load or varying loading can lead to unavoidable gear eccentricity. Although slight eccentricity is common in mechanical systems, the signal fluctuations caused by eccentricity share the same periodicity as those induced by localized gear faults. This presents challenges for fault detection methods based on spectral

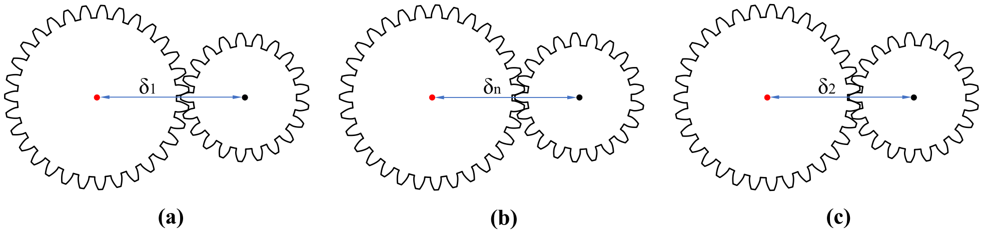

Fig. 5. Center distance of gear meshing: (a) relieved state, (b) normal state, (c) compressed state.

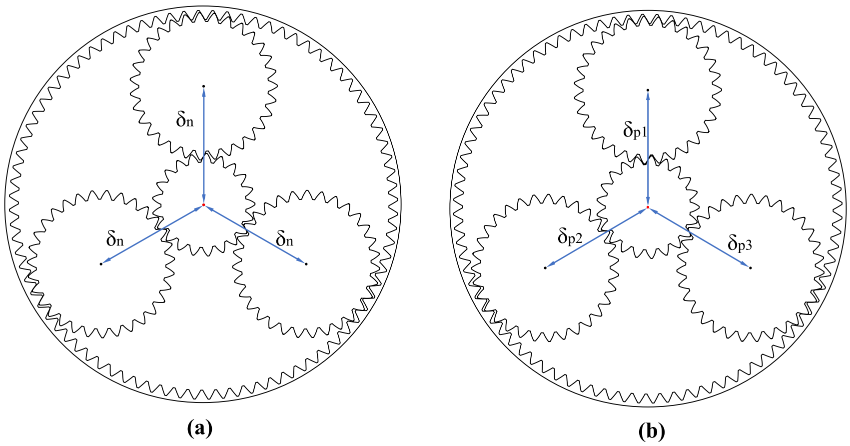

Fig. 6. Comparison of mesh stiffness between healthy condition and sun gear fault condition.

analysis and sideband energy ratio. Therefore, it is necessary to investigate the dynamic behavior and signal characteristics under eccentricity condition to differentiate them from those related with localized faults.

Under ideal condition, the meshing force at the meshing point remains stable throughout the gear rotation, and the center distance between the two meshing gears is constant, denoted as δ_n, as shown in Fig. 5(b). However, when one gear is eccentric, during the rotation of the eccentric gear, the center distance changes, exhibiting two states: one where it increases and one where it decreases, as shown in Fig. 5(a) and (c) with δ_1 and δ_2, respectively. The tooth thickness of the relieved meshing point decreases, whereas the tooth thickness of the compressed meshing point increases. According to Eqs. (8) to (13), the mesh stiffness of the gears in these two states will also decrease and increase, respectively, corresponding to the changes in the center distance. The numerical variation of the time-varying mesh stiffness of the gear approximately follows a sinusoidal fluctuation, with the rotation frequency of the eccentric gear as the period.

In a planetary gear set, when all gears mesh normally without eccentricity, the center distance δ_n between the sun gear and the three planet gears are all equal, as shown in Fig. 6(a). The time-varying mesh stiffness at the three meshing points does not exhibit any amplitude fluctuations. When the sun gear has eccentricity, the center distances between the sun gear and the three planet gears are no longer equal. The center distance with one planet gear δ_1 decreases, resulting in compressed meshing, whereas the center distances with the other two planet gears δ_2 and δ_3 increase, leading to relieved meshing, as shown in Fig. 6(b). The tooth thickness of the compressed sun-planet meshing point increases, whereas the tooth thickness of the other two sun-planet relieved meshing points decrease. As the eccentric sun gear rotates, the compression and relief of the sun-planet meshing points varied periodically. The time-varying mesh stiffness associated with this process changes with the rotational frequency of the sun gear and can be mathematically expressed as:

$$k_{tci} = k_{ti} \sin(f_s + \varphi_i) \tag{14}$$

where k_{tci} represents the time-varying mesh stiffness between the ith planet gear and the sun eccentric gear, i is the index of the planet gear, f_s is the absolute rotation frequency of the sun gear, φ_i is the phase difference of the meshing between the ith planet gear and the sun gear.

The mesh stiffness of the three meshing points under the sun gear eccentricity condition is shown in Fig. 7. It can be observed that the eccentricity affects all meshing points between the sun gear and the three planet gears. When the eccentric sun gear has a fault, the meshing of the faulty tooth with each planet gear causes a decrease in stiffness, and the effect of eccentricity on the time-varying mesh stiffness also persists, as shown in Fig. 8.

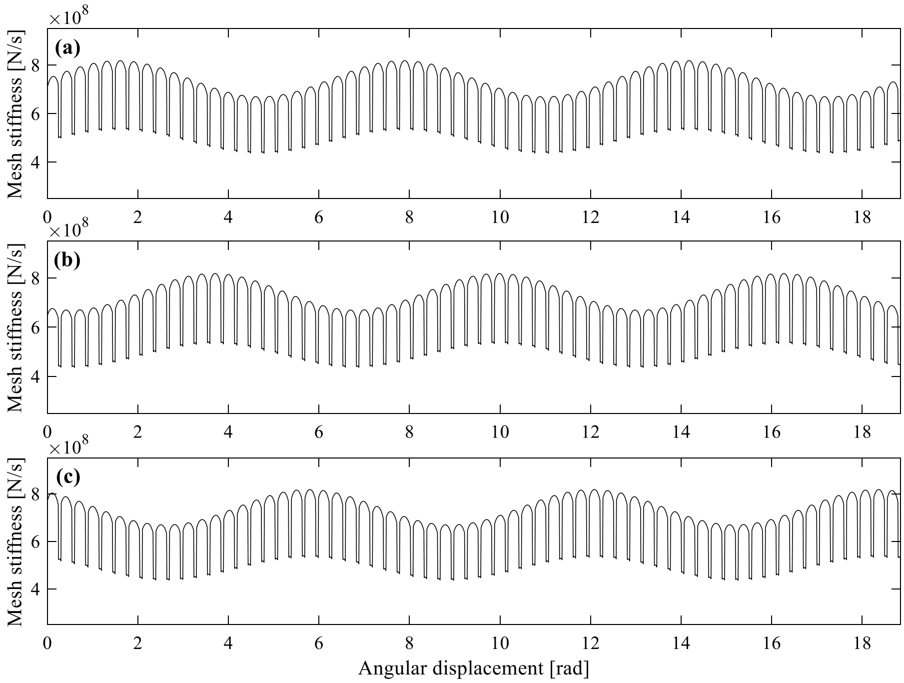

Fig. 7. The time-varying mesh stiffness of the eccentric sun gear with (a) the #1 planet gear, (b) the #2 planet gear and (c) the #3 planet gear.

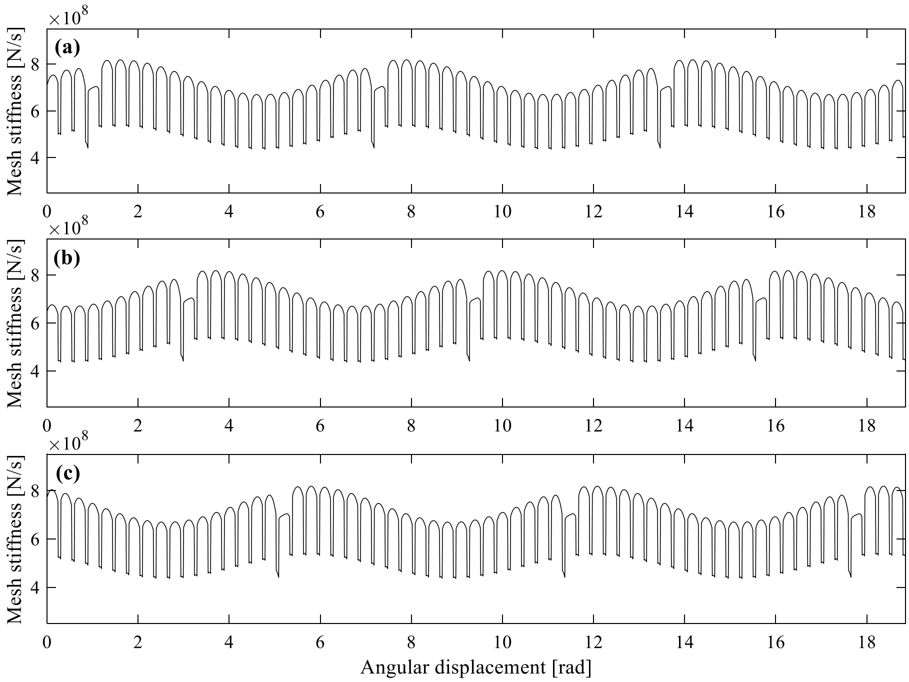

Fig. 8. The time-varying mesh stiffness of the eccentric sun gear with (a) the #1 fault planet gear, (b) the #2 planet gear and (c) the #3 planet gear.

Table 2
Characteristic orders of the planetary gear set.

Items	Order (Carrier as reference)	Order (Sun gear as reference)
Rotation order of the carrier (O_c)	1	0.2
Rotation order of the sun gear (O_s)	5	1
Meshing order (O_m)	84	16.8
Absolute rotation order of the sun gear ($O_s - O_c$)	4	0.8
Sun gear abnormal order (O_{as})	12	2.4

4. Analysis of simulated IAS signal

4.1. Simulation introduction

To investigate the composition and dynamic behavior of IAS in planetary gearboxes and the effect of gear localized fault and gear eccentricity on IAS signals, it is necessary to obtain simulated signals under gear healthy, gear localized fault, gear eccentricity and gear localized fault with eccentricity conditions. Therefore, using the lumped-parameter model described in Section 2, four simulations were conducted on a planetary gear set, with the time-varying mesh stiffness under different conditions serving as internal excitation. The simulations were performed assuming an input speed of 900 r/min and a load torque of 75 Nm. Subsequently, the resulting simulated IAS signals were analyzed.

Based on transmission theory of planetary gear sets [41], Eqs. (15) and (16) can be used to calculate the transmission ratio n and the meshing order O_m of planetary gear set, respectively. Eq. (16) can be used to calculate the absolute rotation order between the sun gear and the carrier, where O_s represents the rotation order of the sun gear, O_c represents the rotation order of the planet carrier, and $O_s - O_c$ represents the absolute rotation order of the sun gear with respect to the carrier. Each planet gear meshes with the faulty tooth of sun gear once in one absolute revolution of the sun gear, resulting in a total of three jitters and the gear fault order given by $O_{rs} = 3(O_s - O_c)$. Because the eccentric sun gear completes one full revolution, speed modulation occurs with each planet gear. The superposition of these modulations from all three planet gears results in the combined modulation order $O_{cs} = O_{rs}$. In this study, the gear fault order O_{rs} and combined modulation order O_{cs} are collectively referred to as abnormal order O_{as}. Using the parameters in Table 1, the characteristic orders can be calculated. These characteristic orders are listed in Table 2,

$$n = (N_r/N_s) + 1 \tag{15}$$

$$O_m = N_r O_c = N_p(O_p + O_c) = N_s(O_s - O_c) \tag{16}$$

$$O_s - O_c = O_c(N_r/N_s) \tag{17}$$

4.2. Simulated IAS signal analysis

The mesh stiffness calculation method described in Section 3 was employed to calculate the time-varying mesh stiffness under four conditions: gear healthy, sun gear localized fault, sun gear eccentricity and gear localized fault with eccentricity. The stiffness were, then, respectively used as excitations for the dynamic model to generate simulated IAS signals corresponding to each condition. In order to display the detail of the IAS fluctuation more clearly and facilitate subsequent order spectrum analysis, the average speed was removed. Because the encoder in this study is mounted on the carrier shaft of the planetary gearbox, the simulated IAS signal of the carrier shaft is used for processing and analysis. The resulting IAS fluctuations for these three conditions are plotted in Fig. 9, presenting data covering 5 cycles (31.4 rad) of carrier rotation T_c.

The simulated IAS fluctuation under gear healthy condition is shown in Fig. 9(a), demonstrating minimal numerical value variations, which result from the alternation of single and double teeth meshing. In contrast, the IAS fluctuation under the sun gear fault condition shown in Fig. 9(b) and (d) exhibits abnormal signal jitters with a periodicity of T_{as} due to the meshing of the faulty tooth. However, the IAS fluctuation under the sun gear eccentricity condition, shown in Fig. 9(c), displays abnormal signal modulation components, also exhibiting a periodicity of T_{as}. All three abnormal conditions exhibit distinct peaks in the IAS signals, making it challenging to distinguish the specific abnormal types based on the waveform.

The order spectra of the IAS fluctuations under gear healthy, sun gear localized fault, sun gear eccentricity and sun gear localized fault with eccentricity conditions are shown in Fig. 10(a), (b), (c) and (d), respectively. Under gear healthy conditions, the order spectrum contains only spectral lines related with meshing order O_m. However, under the sun gear localized fault, sun gear eccentricity, and sun gear localized fault with eccentricity conditions, sideband spectral lines related with O_{as} appear around the meshing order O_m in the order spectrum. Although the distribution and amplitude of the abnormal order spectral lines differ between the sun gear localized fault, sun gear eccentricity and sun gear localized fault with eccentricity conditions, distinguishing these three conditions based solely on the presence of the abnormal order components is challenging.

The envelope spectra of the IAS fluctuations under the four conditions are shown in Fig. 11(a), (b), (c) and (d), respectively. Under the gear healthy conditions, the envelope spectrum does not exhibit any spectral lines related with abnormal order O_{as}. In all the sun gear localized fault, sun gear eccentricity, and sun gear localized fault combined with eccentricity conditions, spectral lines

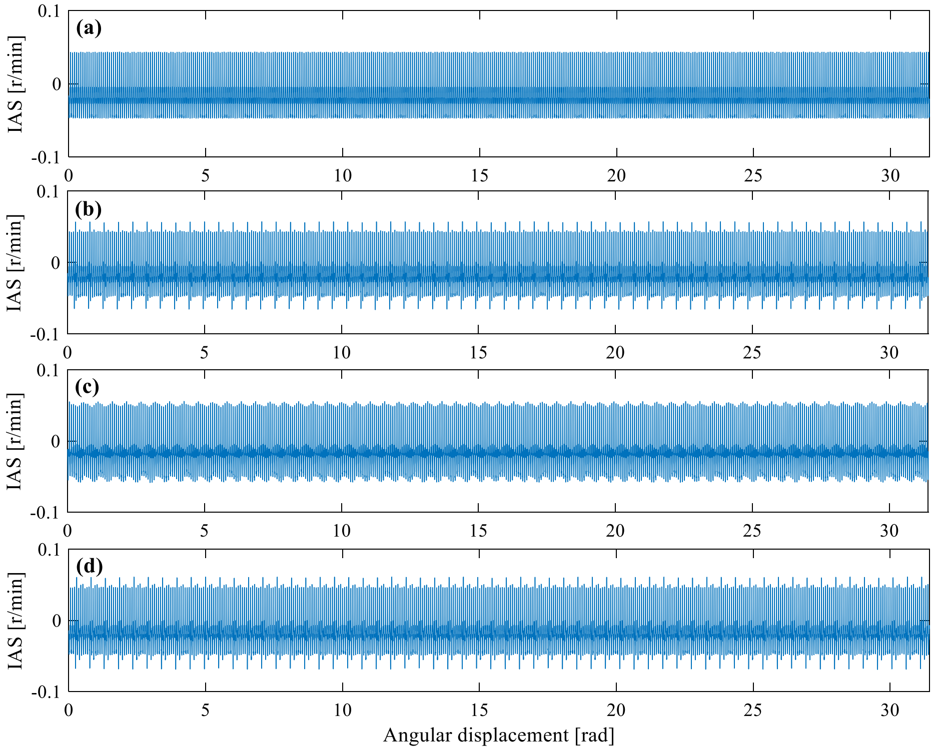

Fig. 9. Simulated IAS signal under (a) healthy gear condition, (b) sun gear localized fault, (c) sun gear eccentricity, and (d) sun gear localized fault combined with eccentricity conditions.

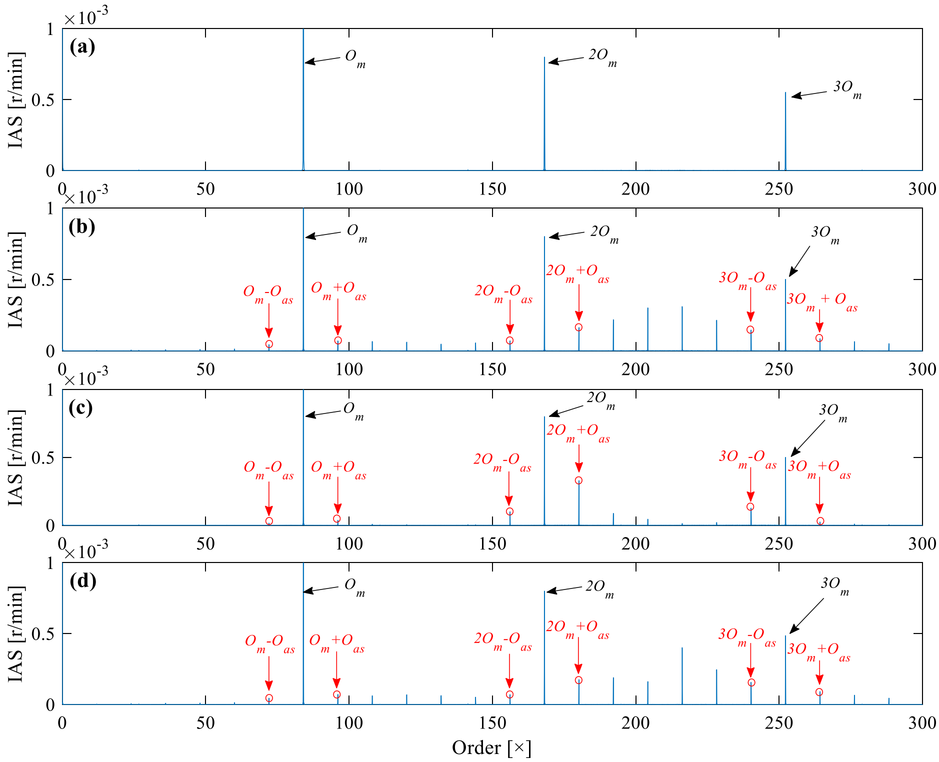

Fig. 10. Order spectra of simulated IAS signals under (a) healthy gear conditions, (b) sun gear localized fault, (c) sun gear eccentricity and (d) sun gear localized fault combined with eccentricity conditions.

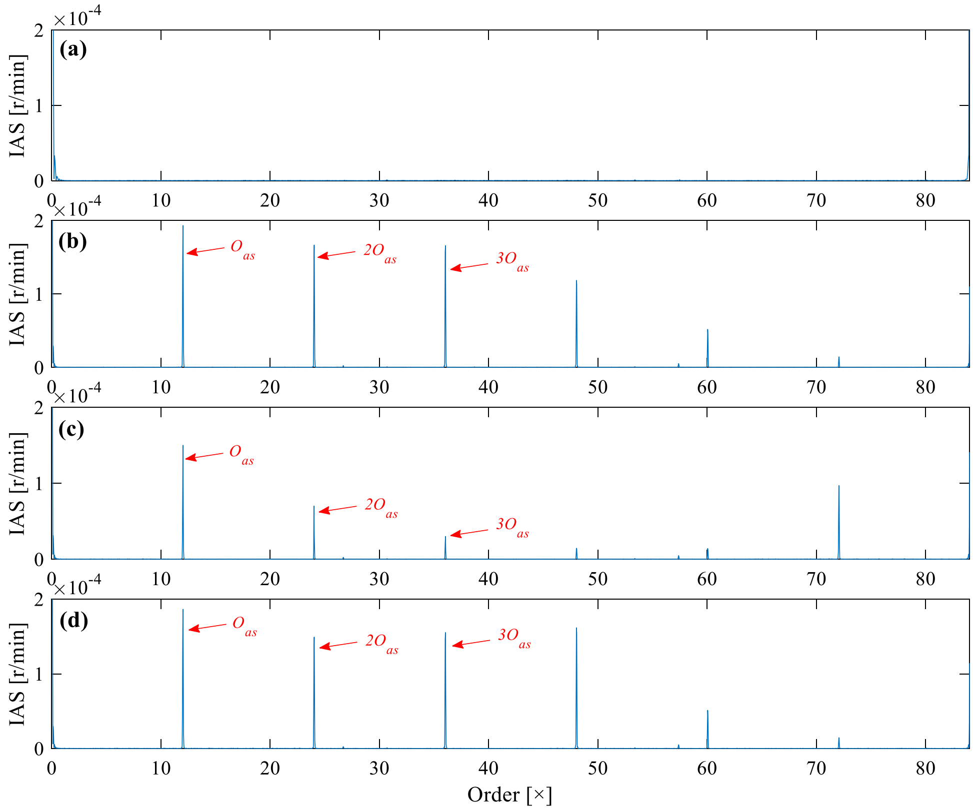

Fig. 11. Envelope spectra of simulated IAS signals under (a) healthy gear conditions, (b) sun gear localized fault, (c) sun gear eccentricity and (d) sun gear localized fault combined with eccentricity conditions.

related to abnormal order O_{as} appear in the envelope spectrum. The presence of abnormal order O_{as} in the envelope spectrum only indicates that a component with a rotational speed corresponding to that order is operating differently from the healthy conditions. However, it cannot determine whether the gear has suffered a localized fault. Therefore, accurately extracting and reconstructing the signal components related to the abnormal order O_{as} is required to analyze the cause of the abnormality in the IAS signals measured.

5. Abnormal-preserving spectral component reconstruction method

5.1. Introduction of reconstruction method

The abnormal components introduced by gear localized fault or gear eccentricity are not dominant in the IAS signal. Despite sharing same characteristic order O_{as} and similar spectral features — such as sidebands around meshing orders and abnormal order-related spectral lines in the envelope spectrum — their amplitude and distribution differ. To effectively highlight these abnormal components, it is important to accurately extract the relevant spectral lines and perform a targeted reconstruction.

Because IAS signal is obtained using an encoder with equal-angle sampling, accurately extracting these spectral components is feasible, and without requiring additional order-tracking techniques typically needed for vibration signals. The main steps of abnormal-preserving spectral component reconstruction include: first, performing a Fourier transform on the IAS signal to obtain its order spectrum information:

$$X(f) = \mathcal{F}\{ias(i)\} = \sum_{n=0}^{N-1} ias(i)e^{-j2\pi ki/N} \tag{18}$$

where, $\mathcal{F}$ represents the Fourier transform, $X(f)$ denotes the corresponding order spectrum, and N is the data length.

The IAS signal is directly obtained using the encoder signal, eliminating the need for equal-angle resampling. As a result, abnormal orders remain fixed, ensuring accurate identification and extraction of fault-related spectral lines. Then, construct the harmonics of the abnormal order O_{as} into an abnormal order sequence f_k, where the harmonics of the meshing order O_m are removed. Although the meshing order O_m is multiple of the abnormal order O_{as}, it is the dominant component in the order information of

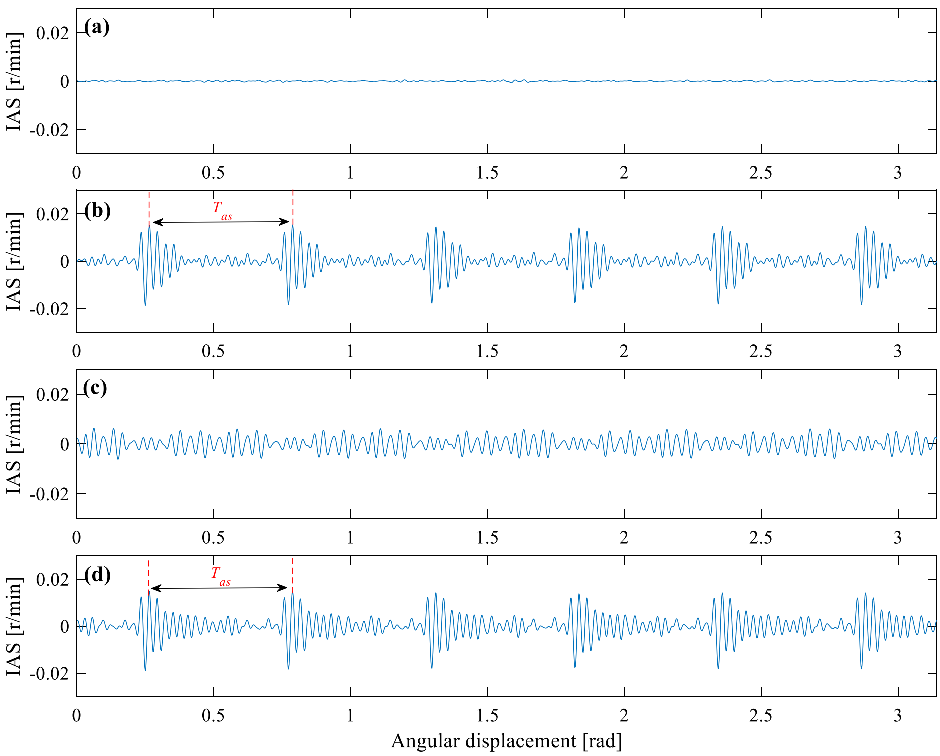

Fig. 12. Reconstructed IAS signals under (a) healthy gear condition, (b) sun gear localized fault, (c) sun gear eccentricity, and (d) sun gear localized fault combined with eccentricity conditions.

both the normal and abnormal conditions. Preserve the abnormal orders in the IAS order spectrum to highlight the spectral lines related to the abnormal orders:

$$X_{\mathrm{re}}(f) = X(f) \cdot \sum_{k=1}^{N} \delta(f - f_k) \tag{19}$$

where $\sigma()$ represents the Dirac delta function, which takes the value of 1 at the abnormal order and 0 at all other orders. Finally, the IAS components related to the abnormal order spectral lines are reconstructed by performing the inverse Fourier transform:

$$ias_{\mathrm{re}}(i) = \frac{1}{N} \sum_{m=0}^{N-1} X_{\mathrm{re}}(f) e^{j2\pi mi/N} \tag{20}$$

5.2. Abnormal component reconstruction and analysis of simulated IAS

The Abnormal-preserving spectral component reconstruction was performed on the simulated IAS under gear healthy, sun gear localized fault, sun gear eccentricity, and sun gear localized fault combined with eccentricity conditions. The resulting reconstructed signals are shown in Fig. 12(a), (b), (c) and (d), respectively. Under gear healthy conditions, the reconstructed IAS exhibits no abnormal jitters or modulation components; under the sun gear localized fault combined with eccentricity conditions, evident periodic jitters appear in the reconstructed IAS, with a period of T_{as}; and under the sun gear eccentricity conditions, the reconstructed IAS exhibits periodic modulation without jitters.

The components corresponding to the same abnormal characteristic order O_{as} in both conditions are effectively extracted and reconstructed, with distinct fault features being enhanced: jitters for localized gear fault and modulation effects for gear eccentricity. The kurtosis values of the raw simulated IAS signals and the reconstructed IAS signals were calculated, as shown in Table 3. This enables a clear differentiation between localized sun gear fault and sun gear eccentricity.

The sideband energy ratio (SER) is defined as the ratio of the sum of the sideband amplitudes on either side of the meshing frequency to the amplitude of the meshing frequency itself [42], and is considered one of the effective indicators for detecting gear faults:

$$SER = \frac{\sum_{i=1}^{M} \{Sideband\ amplitude\}_i}{Meshing\ frequency\text{'s}\ amplitude} \tag{21}$$

where, M is the number of selected sidebands.

Table 3
Kurtosis of raw simulated IAS and reconstructed IAS.

Condition	Kurtosis of raw simulated IAS	Kurtosis of reconstructed simulated IAS
Gear healthy	3.34	3.36
Sun gear localized fault	3.52	6.87
Sun gear eccentricity	3.50	3.46
Sun gear localized fault with eccentricity	3.54	6.23

Table 4
SER values at each meshing order of the simulated signals under different conditions.

Condition	1× meshing order	2× meshing order	3× meshing order
Gear healthy	0	0	0
Sun gear localized fault	0.184	1.044	1.661
Sun gear eccentricity	0.094	0.671	0.542
Sun gear localized fault with eccentricity	0.207	1.053	2.137

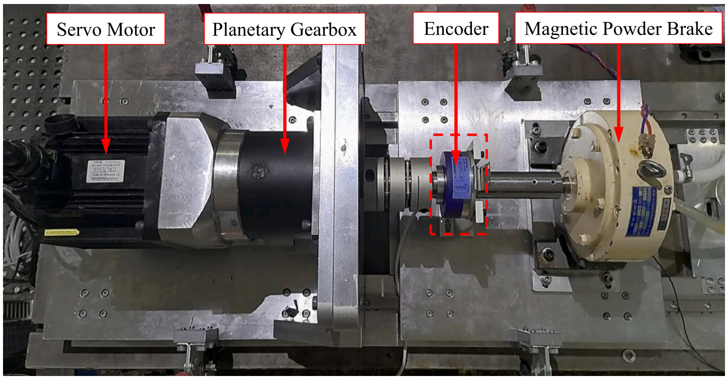

Fig. 13. Planetary gearbox transmission test rig.

Calculate the SER values of the 1×, 2×, and 3× meshing orders based on the order spectra of the simulated IAS signals under the four conditions shown in Fig. 10, respectively, as presented in Table 4. The table shows that under the gear healthy condition, there is no noise or interference from rotational orders, and all SER values are zero. Under the conditions of sun gear localized fault and sun gear localized fault with eccentricity, evident increase in the SER values for the 1×, 2×, and 3× meshing orders is observed compared to the healthy condition, indicating gear faults. However, under the sun gear eccentricity condition, the SER values for the 1×, 2×, and 3× meshing orders also increase. Although these values are not as high as those observed under gear fault conditions, they still interfere with fault detection based on SER. The proposed abnormal-preserving spectral component reconstruction method effectively identifies gear faults from gear shaft eccentricity in terms of the reconstructed signal's waveform and kurtosis, demonstrating the advantages of the proposed approach.

6. Experimental study

The experiments are conducted on a planetary gearbox transmission test rig, illustrated in Fig. 13. This setup includes a servo motor with rated power of 3 kW and rated speed of 1500 r/min, a tested planetary gearbox with nominal power of 2 kW–4 kW and rated speed of 1500 r/min, and a magnetic powder brake with rated torque of 100 Nm. An optical incremental encoder with resolution of 2500 pulses per revolution (PPR) is installed on the output shaft of the planetary gearbox to acquire the IAS signal. The 2500 PPR incremental optical encoder is one of the most commonly used resolutions in industrial applications, offering sufficient resolution to meet the requirements for gear fault detection in planetary gearboxes. A schematic diagram of the test rig is shown in Fig. 14.

In the experiment, the input speed of the sun gear shaft was set to 900 r/min. By setting the input current of the magnetic powder brake to 0.75 A (with rated current of 1 A), the load torque value similar to that in the simulation can be achieved. The time points of the rising edge of the encoder signal are recorded by a high-speed counter using the Field-Programmable Gate Array (FPGA). A tooth spalling fault is artificially introduced on the sun gear to simulate a localized fault, as depicted in Fig. 15.

6.1. Measured IAS signal analysis

The recorded encoder signals under normal, sun gear localized fault conditions are processed using the elapsed time method [43] and differential algorithm to obtain the measured IAS signals. Even if the gears are all healthy, assembly errors, load variations and

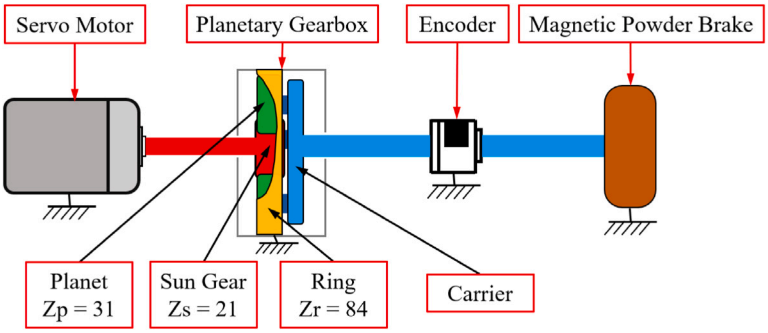

Fig. 14. Schematic diagram of the test rig.

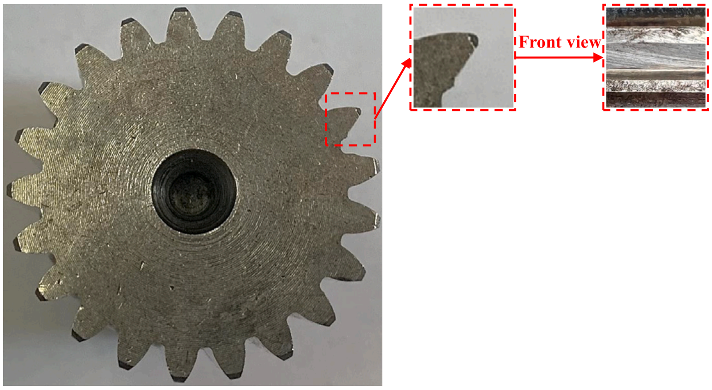

Fig. 15. Faulty sun gear used in the experiment.

other factors can introduce a certain degree of eccentricity into the acquired IAS signal. As a result, obtaining an ideal, interference-free IAS signal becomes challenging. Therefore, in experimental studies, the normal operating conditions should correspond to the gear eccentricity conditions in simulation, and the sun gear fault condition should correspond to the sun gear localized fault combined with eccentricity conditions in simulation. Fig. 16 presents the detail of the measured IAS signals, both showing data for 5 rotations (31.4 rad) of the carrier. Ignoring the noise present in the measured signals, the waveform of the IAS signal under normal conditions, shown in Fig. 16(a), consists of only the single-tooth and double-tooth meshings of the healthy gear teeth, with minor fluctuations caused by their one and two teeth alternating meshing. Additionally, unavoidable manufacturing and assembly errors introduce gear eccentricity, leading to slight amplitude modulation in the signal and generating impact-like peaks in the waveform. The IAS waveform under the sun gear localized fault condition, depicted in Fig. 16(b) exhibit evident jitters. The simulated and measured signals exhibit consistency in their waveforms. This consistency not only validates the validity of the dynamic model but also reflects the actual dynamic behavior of the IAS signal in the planetary gearbox during operation.

The order spectra of the measured IAS signals are shown in Fig. 17. Due to the unavoidable manufacturing and installation errors in practical engineering applications, as well as the influence of couplings and other transmission components, additional rotational order interferences are present in the order spectra. Consequently, in addition to the meshing order components and those related to the rotational order of the sun gear, extra spectral lines are observed. These additional components may be attributed to the rotational orders of the carrier and planet gears, and their harmonics. Specifically, the carrier-related harmonics correspond to multiples of the 1× rotational order, and the characteristic orders related to the planet gears can be calculated based on the gear ratio of the planetary gearbox. Moreover, components corresponding to the motor control frequency and its harmonics may also appear in the spectrum, which are related to the number of pole pairs of the servo motor. In both the normal and sun gear fault conditions, the dominant spectral lines in the order spectrum is the meshing orders. The localized sun gear fault introduces obvious sideband spectral lines related to the abnormal order O_{as} around the meshing order, a key spectral feature of the sun gear fault. However, in the IAS order spectrum under the normal condition, sideband spectral lines related to the abnormal order O_{as} also appear around the meshing order. The presence of this feature may be attributed either to a fault in the sun gear or to the eccentricity of the sun gear shaft. Consequently, relying solely on the appearance of abnormal sidebands as an indicator of sun gear faults is inaccurate. This also leads to the ineffectiveness of methods such as the sideband energy ratio, because both gear fault and gear eccentricity can cause an increase in this ratio.

The envelope order spectra of the measured IAS signals under the normal and the sun gear fault conditions are shown in Fig. 18(a) and (b), respectively. In both conditions, the IAS envelope spectra exhibit evident abnormal order O_{as} harmonics. Although

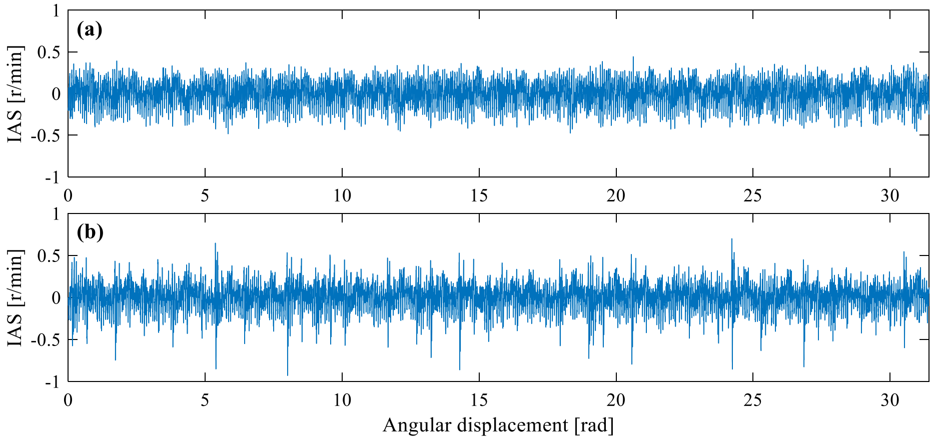

Fig. 16. Waveform of IAS signals under (a) normal, and (b) sun gear fault conditions.

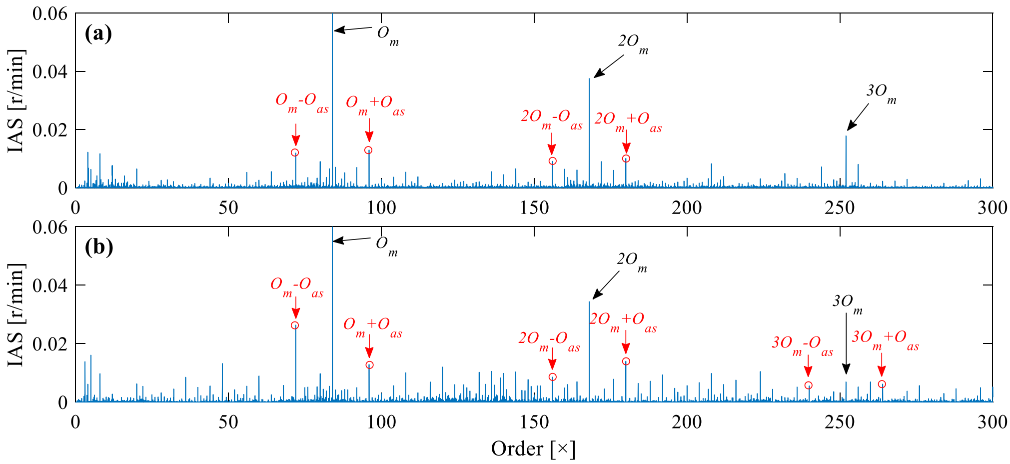

Fig. 17. Order spectra of measured IAS signals under (a) normal and (b) sun gear fault conditions.

Table 5
Kurtosis of raw measured IAS and reconstructed IAS.

Condition	Kurtosis of raw measured IAS	Kurtosis of reconstructed measured IAS
Normal	3.72	3.81
Sun gear fault	4.43	6.24

the amplitude and distribution of the harmonic spectral lines are more prominent in the sun gear fault condition, the presence of this feature in both conditions poses challenges for accurately identifying the sun gear fault.

6.2. Abnormal component reconstruction and analysis of measured IAS

The measured IAS signals under both normal and sun gear fault conditions were processed using the proposed abnormal-preserving spectral component reconstruction method. The resulting reconstructed signals are shown in Fig. 19(a) and (b), respectively. Under normal condition, the reconstructed IAS exhibits no abnormal jitters component; under the sun gear fault conditions, evident periodic jitters appear in the reconstructed IAS, with a period of T_{as}. The kurtosis values of the original IAS signals and the reconstructed IAS signals were calculated, as shown in Table 5. It was observed that the kurtosis value of the IAS signal under the sun gear fault condition significantly increased after reconstruction, indicating that the impacts corresponding to the localized gear fault in the original signal were effectively extracted.

The SER values for the 1×, 2×, and 3× meshing orders from the order spectra of the measured IAS signals under the normal and sun gear fault conditions are calculated and presented in Table 6. The SER values under the sun gear fault condition are higher

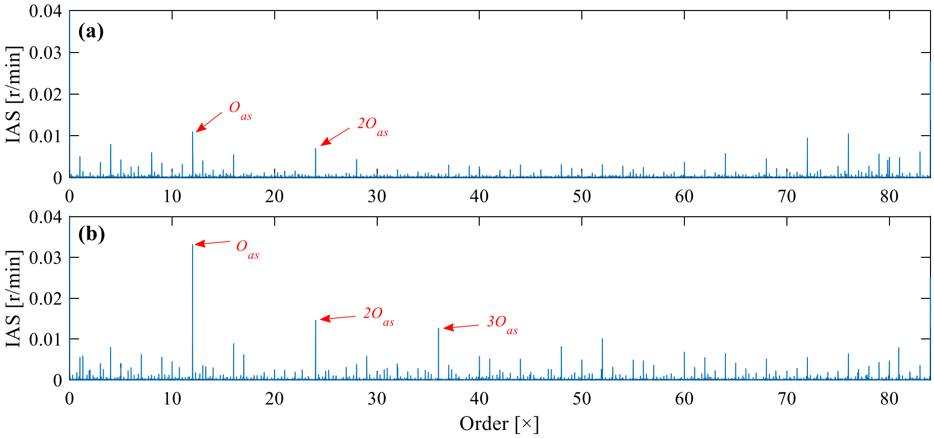

Fig. 18. Envelope order spectra of measured IAS signals under (a) normal, and (b) sun gear fault condition.

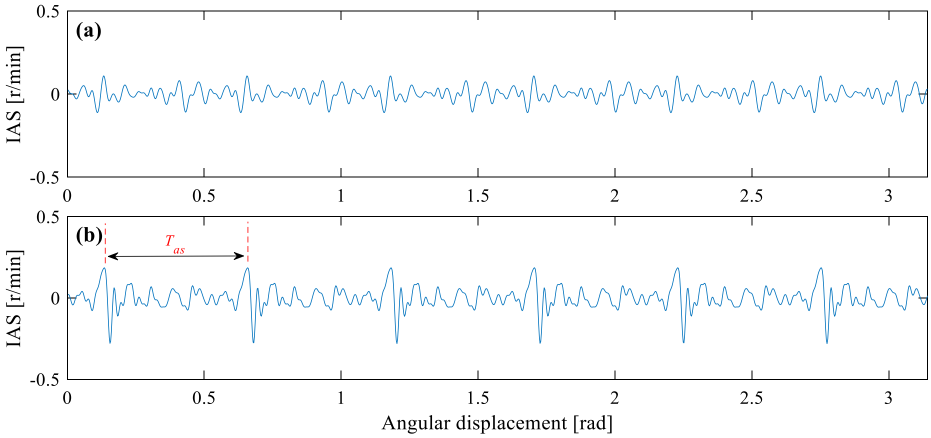

Fig. 19. Reconstructed measured IAS signal under (a) normal and (b) sun gear fault conditions.

Table 6
SER values at each meshing order of the measured signals under different conditions.

Condition	1× meshing order	2× meshing order	3× meshing order
Normal	0.532	0.776	0.943
Sun gear fault	1.308	1.647	1.985

than those under the normal condition. However, relying solely on the SER values in the normal condition cannot determine the gear's health, because the SER values are not negligible. Evident signal jitter is observed in the reconstructed IAS signals obtained using the abnormal component. Additionally, the kurtosis value of the reconstructed signal under the sun gear fault condition is significantly higher than that under the normal condition, demonstrating a more effective fault identification capability compared to the SER indicator.

7. Conclusion and discussion

A modified torsional dynamic model in the angular domain for planetary gearboxes has been developed through a comprehensive torque balance analysis. By analyzing the time-varying mesh stiffness under gear healthy, sun gear localized fault, and gear eccentricity conditions, and incorporating these conditions as variables into the dynamic model, the simulated IAS signals can be obtained. The correctness of the model has been verified by analyzing simulated and experimentally measured IAS signals. Furthermore, the influence of gear localized fault and gear eccentricity on the dynamic behavior of IAS has been examined. To enhance fault identification, an abnormal-preserving spectral component reconstruction method has been proposed to extract and identify gear fault. The key findings of this paper can be summarized as follows:

(1) Torque balance analysis of the gear under localized faults and shaft eccentricity conditions reveals that both conditions influence the time-varying mesh stiffness. A localized gear fault causes a sudden drop in mesh stiffness when the faulty tooth meshes, whereas gear shaft eccentricity introduces a periodic modulation to the time-varying mesh stiffness.

(2) The dynamic behavior of the signal components induced by localized gear faults and gear eccentricity exhibits the same periodicity, resulting in identical characteristic orders. However, the amplitude and distribution of the spectral lines corresponding to these characteristic orders differ between the two conditions in the order spectrum.

(3) Accurate extraction and reconstruction of the spectral lines corresponding to abnormal characteristic orders enable effective differentiation between localized gear faults and gear eccentricity. The IAS signal reconstructed for localized gear faults exhibits evident periodic jitters and a significant increase in kurtosis, whereas the reconstructed IAS signal for gear shaft eccentricity does not exhibit these characteristics.

CRediT authorship contribution statement

Jiawei Fan: Writing – original draft, Validation, Software, Methodology, Investigation, Formal analysis. **Yu Guo:** Writing – review & editing, Supervision, Resources, Funding acquisition. **Enrico Zio:** Writing – review & editing. **Hugo Andre:** Writing – review & editing, Validation. **Jing Na:** Writing – review & editing. **Xingchao Yin:** Writing – review & editing, Validation.

Declaration of competing interest

The authors declare that they have no known competing financial interests or personal relationships that could have appeared to influence the work reported in this paper.

Acknowledgments

We gratefully acknowledge the support from the National Natural Science Foundation of China (Grant No. 52165067), the Yunnan Fundamental Research Projects (grant No. 202501AS070116), and the China Scholarship Council (CSC) High-Level University Postgraduate Program (Grant No. 202408530186).

Data availability

The authors do not have permission to share data.

References

[1] T. Wang, Q. Han, F. Chu, Z. Feng, Vibration based condition monitoring and fault diagnosis of wind turbine planetary gearbox: A review, Mech. Syst. Signal Process. 126 (2019) 662–685.
[2] W. Wu, D. Prescott, R. Remenyte-Prescott, A. Saleh, M.C. Ruano, An asset management modelling framework for wind turbine blades considering monitoring system reliability, Reliab. Eng. Syst. Saf. (2024) 110478.
[3] L. Ryali, D. Talbot, A dynamic load distribution model of planetary gear sets, Mech. Mach. Theory 158 (2021) 104229.
[4] C. Wang, L. Yu, H. Wang, B. Zhang, H. Luo, Fault modulation mechanism and kinematic modeling of planetary gear with local fault, J. Sound Vib. (2024) 118572.
[5] Y. Lei, D. Han, J. Lin, Z. He, Planetary gearbox fault diagnosis using an adaptive stochastic resonance method, Mech. Syst. Signal Process. 38 (2013) 113–124.
[6] K. Shao, Y. He, Z. Xing, B. Du, Detecting wind turbine anomalies using nonlinear dynamic parameters-assisted machine learning with normal samples, Reliab. Eng. Syst. Saf. 233 (2023) 109092.
[7] X. Yu, Z. Feng, M. Liang, Analytical vibration signal model and signature analysis in resonance region for planetary gearbox fault diagnosis, J. Sound Vib. 498 (2021) 115962.
[8] P. Zhou, Z. Peng, S. Chen, Z. Tian, M.J. Zuo, Sinusoidal FM patterns of fault-related vibration signals for planetary gearbox fault detection under non-stationary conditions, Mech. Syst. Signal Process. 155 (2021) 107623.
[9] I. Manarikkal, F. Elasha, D. Mba, Diagnostics and prognostics of planetary gearbox using CWT, auto regression (AR) and K-means algorithm, Appl. Acoust. 184 (2021) 108314.
[10] W. Teng, Y. Liu, Y. Huang, L. Song, Y. Liu, Z. Ma, Fault detection of planetary subassemblies in a wind turbine gearbox using TQWT based sparse representation, J. Sound Vib. 490 (2021) 115707.
[11] Y. Yang, N. Hu, Y. Li, Z. Cheng, G. Shen, Dynamic modeling and analysis of planetary gear system for tooth fault diagnosis, Mech. Syst. Signal Process. 207 (2024) 110946.
[12] F. Elasha, M. Greaves, D. Mba, D. Fang, A comparative study of the effectiveness of vibration and acoustic emission in diagnosing a defective bearing in a planetary gearbox, Appl. Acoust. 115 (2017) 181–195.
[13] J. Yao, C. Liu, K. Song, X. Zhang, D. Jiang, Fault detection of complex planetary gearbox using acoustic signals, Measurement 178 (2021) 109428.
[14] X. Chen, Z. Feng, Induction motor stator current analysis for planetary gearbox fault diagnosis under time-varying speed conditions, Mech. Syst. Signal Process. 140 (2020) 106691.
[15] Y. Guo, L. Zhao, X. Wu, J. Na, Vibration separation technique based localized tooth fault detection of planetary gear sets: A tutorial, Mech. Syst. Signal Process. 129 (2019) 130–147.
[16] Y. Li, K. Ding, G. He, X. Yang, Vibration modulation sidebands mechanisms of equally-spaced planetary gear train with a floating sun gear, Mech. Syst. Signal Process. 129 (2019) 70–90.
[17] J. Fan, Y. Guo, J. Na, X. Yin, Gear tooth fault detection in servo motor transmission chain using the built-in encoder of servo motors, IEEE Trans. Instrum. Meas. 73 (2024) 3521509.

[18] B. Li, X. Zhang, A new strategy of instantaneous angular speed extraction and its application to multistage gearbox fault diagnosis, J. Sound Vib. 396 (2017) 340–355.
[19] G. Bruand, F. Chatelain, P. Granjon, N. Martin, C. Duret, Reconstructing shaft orbit using angle measurement to detect bearing faults, Mech. Syst. Signal Process. 139 (2020) 106561.
[20] X. Chen, Y. Guo, J. Na, Instantaneous-angular-speed-based synchronous averaging tool for bearing outer race fault diagnosis, IEEE Trans. Ind. Electron. 70 (2022) 6250–6260.
[21] X. Yang, Y. Guo, H. Wang, Encoder signal analysis and its application in gear fault detection, IEEE Trans. Instrum. Meas. 73 (2023).
[22] C. Peeters, J. Antoni, Q. Leclère, T. Verstraeten, J. Helsen, Multi-harmonic phase demodulation method for instantaneous angular speed estimation using harmonic weighting, Mech. Syst. Signal Process. 167 (2022) 108533.
[23] M. Zhao, X. Jia, J. Lin, Y. Lei, J. Lee, Instantaneous speed jitter detection via encoder signal and its application for the diagnosis of planetary gearbox, Mech. Syst. Signal Process. 98 (2018) 16–31.
[24] Q. Zeng, G. Feng, Y. Shao, F. Gu, A.D. Ball, Planetary gear fault diagnosis based on an instantaneous angular speed measurement system with a dual detector setup, IEEE Access 8 (2020) 66228–66242.
[25] Z. Feng, A. Gao, K. Li, H. Ma, Planetary gearbox fault diagnosis via rotary encoder signal analysis, Mech. Syst. Signal Process. 149 (2021) 107325.
[26] Z. Liang, T. Wang, F. F. Chu, X. Wang, Cut-off point (COP) for early gear fault diagnosis via meshing impact modulation (MIM) analysis, J. Sound Vib. 590 (2024) 118525.
[27] M. Luo, H. André, Y. Guo, Y. Peng, Analysis of contact behaviours and vibrations in a defective deep groove ball bearing, J. Sound Vib. 570 (2024) 118104.
[28] X. Liang, M.J. Zuo, Z. Feng, Dynamic modeling of gearbox faults: A review, Mech. Syst. Signal Process. 98 (2018) 852–876.
[29] N. Lu, S. Huang, Y. Li, B. Jiang, O. Kaynak, E. Zio, Dynamic weight-based accelerated test modeling for fault degradation and lifetime analysis, Reliab. Eng. Syst. Saf. 252 (2024) 110405.
[30] X. Liang, M.J. Zuo, M.R. Hoseini, Vibration signal modeling of a planetary gear set for tooth crack detection, Eng. Fail. Anal. 48 (2015) 185–200.
[31] H. Han, Z. Zhao, H. Tian, H. Ma, Y. Yang, X. Li, Fault feature analysis of planetary gear set influenced by cracked gear tooth and pass effect of the planet gears, Eng. Fail. Anal. 121 (2021) 105162.
[32] F. Jiang, K. Ding, G. He, Y. Sun, L. Wang, Vibration fault features of planetary gear train with cracks under time-varying flexible transfer functions, Mech. Mach. Theory 158 (2021) 104237.
[33] X. Liang, M.J. Zuo, T.H. Patel, Evaluating the time-varying mesh stiffness of a planetary gear set using the potential energy method, Proc. Inst. Mech. Eng. C 228 (2014) 535–547.
[34] X. Liang, H. Zhang, M.J. Zuo, Y. Qin, Three new models for evaluation of standard involute spur gear mesh stiffness, Mech. Syst. Signal Process. 101 (2018) 424–434.
[35] J. Hu, N. Hu, Y. Yang, L. Zhang, G. Shen, Nonlinear dynamic modeling and analysis of a helicopter planetary gear set for tooth crack diagnosis, Measurement 198 (2022) 111347.
[36] Y. Qin, Q. Li, S. Wang, P. Cao, Dynamics modeling of faulty planetary gearboxes by time-varying mesh stiffness excitation of spherical overlapping pittings, Mech. Syst. Signal Process. 210 (2024) 111162.
[37] G. Zhao, Z. Jiang, Study on torsional stiffness of engine crankshaft, in: 2009 International Forum on Computer Science-Technology and Applications, Vol. 3, 2009, pp. 431–435.
[38] M.S. Tavakoli, D.R. Houser, Optimum profile modifications for the minimization of static transmission errors of spur gears, J. Mech. Transm. Autom. Des. 108 (1986) 86–94.
[39] A. Kahraman, R. Singh, Interactions between time-varying mesh stiffness and clearance non-linearities in a geared system, J. Sound Vib. 146 (1991) 135–156.
[40] H.H. Lin, R.L. Huston, J.J. Coy, On dynamic loads in parallel shaft transmissions: Part I—Modelling and analysis, J. Mech. Transm. Autom. Des. 110 (1988) 221–225.
[41] D.G. Lewicki, P.D. Samuel, J.K. Conroy, D.J. Pines, Planetary transmission diagnostics, NASA CR 2004.
[42] M. Zhang, H. Cui, Q. Li, J. Liu, K. Wang, Y. Wang, An improved sideband energy ratio for fault diagnosis of planetary gearboxes, J. Sound Vib. 491 (2021) 115712.
[43] Y. Li, F. Gu, G. Harris, A. Ball, N. Bennett, K. Travis, The measurement of instantaneous angular speed, Mech. Syst. Signal Process. 19 (2005) 786–805.